Nuclear Science and Techniques (2026) 37:58
https://doi.org/10.1007/s41365-026-01893-7

Prototype design of satellite payload for neutron spectrum acquisition

Xiao-Li Wang[1] · Shu-Cheng Shi[1] · Chen-Yao Han[1] · Yi-Ming Ma[2] · Quan-Qi Shi[1] · Shuai Wang[2] · Jiao Feng[2]

Received: 1 October 2024 / Revised: 26 March 2025 / Accepted: 21 May 2025 / Published online: 28 January 2026

Abstract

In recent years, there have been fewer missions to detect neutrons in low Earth orbits (LEO), and the data obtained have been extremely limited. Studying the distribution of the neutron energy spectrum in LEO satellites through detection can help solve three major scientific problems: the source of particles in the inner radiation belt, information on solar-accelerated particles, and the proportion of neutrons from different sources in near-Earth space. The detection efficiency and accuracy of neutrons are affected by charged and primary particles in the environment and secondary neutrons produced by the spacecraft itself, which has been a hot research topic. The neutron spectrometer developed in this study adopts two combinations of 15 silicon detectors in terms of detector type and arrangement, which are used for neutron detection via the nuclear reaction method and recoil proton method, respectively, in which a 27 μm-thick ^{6}LiF conversion layer is used for thermal neutron detection up to 0.4 eV and a 300 μm-thick high-density polyethylene conversion layer is used for fast-neutron detection up to 14 MeV and below. The design of the detector set can also remove the influence of primary charged particles and secondary neutrons in the detection environment to a certain extent, thereby improving the accuracy of neutron detection. In this study, the neutron spectrometer hardware, firmware, software design, and basic performance of the front-end readout chip SKIROC2A were tested. The readout circuit of each channel baseline ADC code was less than 17; thus, the channel consistency was good. The RMS noise of the channel baseline was only 7.1 mV and exhibited good stability. The maximum number of events that could be processed per second is 75. The overall power consumption was 3 W, the weight was 792 g, and the volume was less than 1 dm^3. Furthermore, the neutron spectrometer was tested for principle and detection efficiency using various neutron sources, such as ^{241}Am-Be neutron source, 2.5 MeV neutron beam, and 14 MeV neutron beam, and the experiments were analyzed with corresponding simulations. The experimental data and simulation results were in good agreement and met the design requirements. The intrinsic detection efficiency of the probes used in the neutron spectrometer was 1.05 % for 14 MeV fast neutrons.

Keywords Neutron spectrometer · Satellite payload · Prototype design · Geant4 · SKIROC2A

1 Introduction

There are several sources of neutrons in the near-Earth space. For example, galactic cosmic rays [1] can reach the vicinity of the Earth and produce neutrons, and a high-energy solar particle event [2] reaching the Earth's atmosphere [3] triggers secondary neutrons, which are detected by ground-based neutron monitors. Secondary neutrons are produced by the interaction of spacecraft materials with solar energetic protons, galactic cosmic rays, and locally trapped protons in radiation belts [4], solar neutrons are produced by the interaction of solar protons and heavy ions with the Sun's atmosphere [5, 6], and lightning neutrons are produced by the interaction of lightning energetic gamma rays with the Earth's atmosphere [7, 8]. The detection of neutrons in

This work was supported by the National Natural Science Foundation of China (NSFC) (Nos. 42225405 and U2106202).

✉ Chen-Yao Han
chenyao.han@mail.sdu.edu.cn

✉ Quan-Qi Shi
sqq@sdu.edu.cn

[1] Shandong Key Laboratory of Space Environment and Exploration Technology, School of Space Science and Technology, Institute of Space Sciences, Shandong University, Weihai 264209, China

[2] School of Airspace Science and Engineering, Shandong University, Weihai 264209, China

near-Earth space using neutron spectrometers can help solve three major scientific problems. These include the study of the radiation sources of particles in inner radiation belts [9], the mechanism of solar neutrons in the study of particles accelerated by solar flares [10], and the percentage of neutrons from different sources in near-Earth space, which can be analyzed in comparison with lightning observation data on the ground.

The current mainstream view is that cosmic-ray albedo neutron decays are one of the sources of protons in the inner radiation belts, although it was previously thought that the electron fluxes at different locations in the radiation belts differed significantly and that there would be other sources [11]. However, the data measured from low Earth orbit (LEO) by Li et al. [12] in 2017 show that albedo neutron decay is a stable source of electrons in radiation belts. Therefore, neutron spectrometer data are promising for providing reliable observational evidence to supplement or explain this theory. Current observations of solar neutron events are mainly based on the construction of large neutron detectors in high- and low-latitude areas on the ground [13]. A neutron spectrometer can directly detect solar neutron events outside the Earth's atmosphere, thus eliminating the influence of the Earth's atmosphere and helping detect weaker solar neutron events [14] with clearer detection signals. It can even observe solar neutron events during periods of relatively infrequent solar activity. In addition, neutron spectrometers can detect neutrons produced by Earth's lightning, and in combination with lightning observation base station data on the ground [15], study the contribution of lightning to neutrons in near-Earth space [16, 17].

As the radiation environment of LEO is more complex, there are several types of high-energy charged primary particles that undergo various types of nuclear reactions with the neutron detector itself to produce secondary neutrons. Neutron detection must exclude the influence of various types of errors; therefore, in recent years, there have been fewer neutron detection missions for LEO. In 1989, Keith et al. [18] used various neutron detectors to detect neutrons in LEO. For thermal neutrons, a 50 μm Gd shield and other elements with a large neutron capture cross section were used. The fast neutrons were measured using a Bonner ball detector. The complex structure of a detector results in a bulky system. In 1991, Dudkin et al. placed several neutron detectors on the Mir space station to measure the neutron energy spectrum in LEO [19], relying on nuclear latex and organic scintillator detectors containing ^{6}Li with a more conventional data processing system that could not satisfy the scenario of real-time data and a large neutron differential flux. In the same year, Korf et al. [20] used organic scintillators to detect neutron differential flux spectra in the Earth's atmosphere, using plastic scintillator wraps for anti-consistency. However, the plastic scintillator must be shielded from gamma rays, resulting in a larger volume and poorer energy resolution. In 2001, Lyagushin et al. [21] used a nuclear latex detector and nuclear fission foil to detect LEO neutrons inside the Mir space station module, which is more efficient for fast neutrons but sensitive to gamma-ray interference and can easily lead to false triggering. A certain amount of fissile materials is typically required, resulting in large detector sizes. In the same year, Matsumoto et al. [22] used a Bonner ball detector to detect neutrons on the ISS, in which the ^{3}He tube detector used was large and fragmented, which is not suitable for space payload miniaturization. Moreover, the detection efficiency of the ^{3}He tube detector for neutrons varies with the neutron energy; hence, the precalibration work is tedious. The China Space Station has installed an energy particle detector, which features the innovative use of CLYC (Cs_2LiYCl_6:Ce) as a neutron measurement sensor [23, 24]. This was the first application of this material in space detection.

Current space neutron detection equipment is generally excessively complex and bulky, resulting in high power consumption, which is not suitable for long-term data acquisition on compact satellites. With the development of semiconductor detectors [25, 26], integrated forward chips [27, 28], and high-speed data acquisition and processing systems [29, 30], it is possible for space neutron detection payloads to achieve long-time operation, high detection efficiency, and high anti-jamming capability to ensure low-power miniaturization [31, 32].

For neutron detection applications in LEO satellites, a neutron spectrometer [33, 34] has been constructed by our group. The neutron spectrometer is based on Si detectors [35, 36], using ^{6}LiF [37, 38] and high-density polyethylene (HDPE) [39, 40] as the neutron conversion layer for the detection of thermal neutrons (< 0.4 eV) and fast neutrons (< 14 MeV). The power consumption of the neutron spectrometer as a whole is 3 W, which, combined with the power consumption assigned by the satellite, is expected to be consumed continuously for one year in orbit. The overall weight was 792 g, and its volume was less than 1 dm^3. The neutron spectrometer onboard the "Weiming-1" CubeSat was launched in January 2024, in a Sun-synchronous orbit at an altitude of approximately 530 km. On-orbit data from neutron spectrometers have been accumulated and processed.

2 System composition

2.1 Detector selection

Si detectors have a low density, low leakage current, small size, and high-energy resolution. They are widely used for particle detection. Therefore, in this study, 15 Si detectors

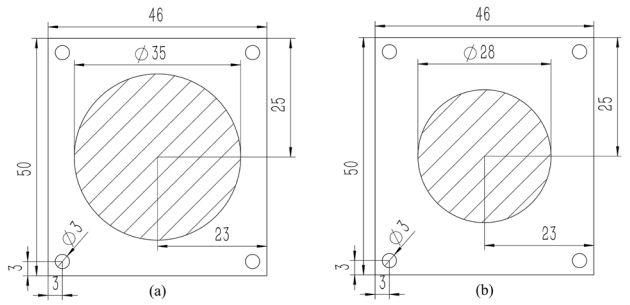

Fig. 1 Detector dimensions: **a** 35 mm, and **b** 28 mm

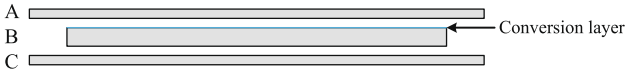

Fig. 2 (Color online) Schematic of anti-coincidence structure

with the effective circular area diameters of 35 mm and 28 mm and a thickness of 300 μm were designed as the detectors of the particle detection system. It can be ensured that particles in the predetection energy range produce sufficient deposition energy in the detectors [41, 42]. The package dimensions of the two Si detectors are shown in Fig. 1.

2.2 Arrangement of detectors

For neutron detection in space, the radiation environment in which the detector is located is complex. Both charged particles and neutrons exist in space; therefore, the interference of charged particles must be eliminated using the anti-coincidence method. Figure 2 shows a schematic of the anti-coincidence structure, where the upper and lower detectors have larger areas, whereas the middle detector has a smaller area. Blue represents the conversion layer [42]. Anti-coincidence indicates that, if there is a signal in detectors A or C at the same moment, the signal in detector B at this moment is removed.

A neutron spectrometer detects thermal and fast neutrons with energies up to 14 MeV. To improve detection efficiency and remove the influence of charged particles, the thermal neutron section used six detectors and Gd shielding consisting of an anti-coincidence detector set. The fast-neutron section used nine detectors, one of which was shared by the fast and thermal neutrons. The arrangement of the neutron spectrometer detector is illustrated in Fig. 3, with 15 silicon semiconductor detectors [42].

There were 15 silicon semiconductor detectors with a thickness of 300 μm. Detector No. 6 was covered with a 300 μm-thick HDPE conversion layer. Detectors Nos. 11 and 14 were covered with a 27 μm-thick LiF conversion layer. Detectors Nos. 3, 4, 5, 7, 8, 9, 11, and 14 had an effective circular area with a diameter of 28 mm. Detectors Nos. 1, 2, 6, 10, 12, 13, and 15 had an effective circular area with a diameter of 35 mm.

Detector No. 1 was used to identify the direction of the incoming probe particles. Detectors No. 2–10 were fast-neutron detectors, of which Nos. 3, 4, 5, and Nos. 7, 8, 9 had the same thickness and effective area; the only difference was that there was a 300 μm-thick HDPE fast-neutron converter layer in front of Nos. 7, 8, and 9. Moreover, the detectors No. 3, 4, and 5 could detect signals generated by galactic cosmic rays or other secondary neutrons, whereas the recoil proton detectors Nos. 7, 8, and 9 could also detect the recoil proton signals generated by orbital neutrons passing through the HDPE conversion layer. Therefore, under the anti-coincidence condition, the recoil proton spectrum

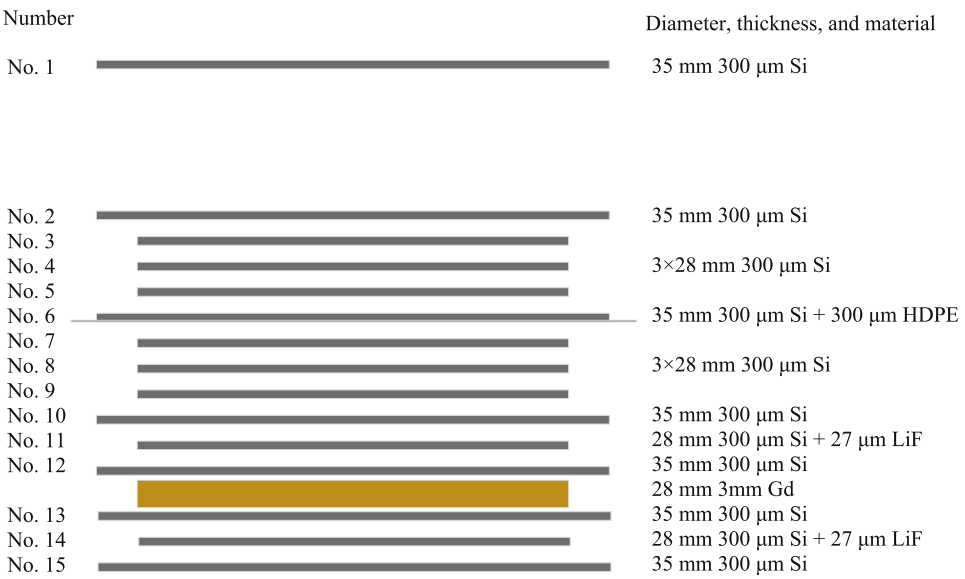

Fig. 3 (Color online) Neutron spectrometer 15-chip detector set

could be obtained by subtracting the total energy spectra of detectors Nos. 7, 8, and 9 and silicon detectors Nos. 3, 4, and 5, which could effectively reduce the influence of background signals on the measurements and improve the accuracy of the neutron energy spectrum inversion. The thickness of the three-layer recoil proton detector was approximately 900 μm, which allowed the complete deposition of protons up to 14 MeV, considering oblique incidence. Fast neutrons were detected using the recoil proton method, and the fast-neutron energy spectrum was obtained using the least-squares method, which is a neutron inversion algorithm [43]. The simulation results using Geant4 are shown in Fig. 4.

Detectors No. 10–15 were thermal neutron detectors. Detectors Nos. 10, 12, 13, and 15, which had larger areas, were used as anti-coincidence detectors; thus, charged-particle signals in a wide range of stereo angles could be removed by anti-coincidence. A 3 mm-thick sheet of Gd was placed between detectors Nos. 12 and 13 to absorb thermal neutrons; thus, detector No. 11 with the ^{6}LiF coating could record the signal counts generated by the reaction of neutrons in the omnipotent band with ^{6}LiF. Detector No. 14, with ^{6}LiF coating, mainly recorded the counts of signals generated by the reaction of neutrons other than thermal neutrons with ^{6}LiF. The thermal neutron flux in orbit could be obtained by dividing the difference in counts between the two detectors by the detection efficiency. In addition, to distinguish the source direction of thermal neutrons in LEO to a certain extent, a piece of 3 mm-thick Gd was placed around the detector array, except for the remaining five faces of the open side, to block the thermal neutrons from other directions [43], and the specific position of Gd is shown in Fig. 5.

The blue part represents the 3 mm-thick Gd placed on the five faces around the detector combination. As the capture

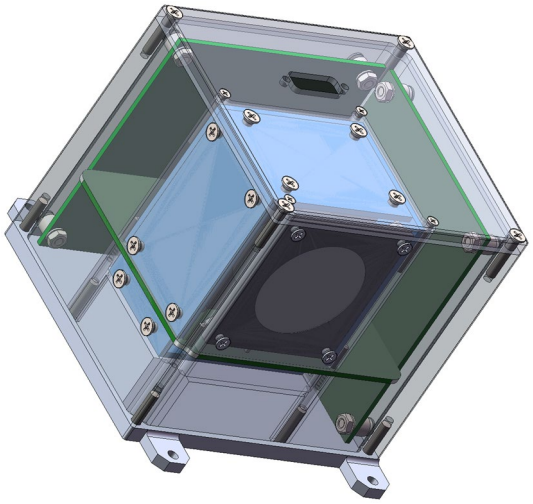

Fig. 5 (Color online) Gd placed on five faces around the detector

cross sections of thermal neutrons are different for different Gd isotopes and the reaction cross sections of neutrons and ^{6}Li are different for different energies, to analyze the effect of Gd on thermal neutron detection at different energies, Si detectors with LiF coatings that are blocked by Gd and those that are not were simulated using Geant4 simulations to study the variation in the detection efficiency of the detector for thermal neutrons with thermal neutron energy in both cases [43], as shown in Fig. 6.

The orange data points are the detection efficiency of detector No. 11 for different neutron energies as a function of neutron energy, the blue data points are the detection efficiency of detector No. 14 for different neutron energies as a function of neutron energy, and the gray lines are the reaction cross sections of ^{6}Li (N,T)^{4}He as a function of neutron

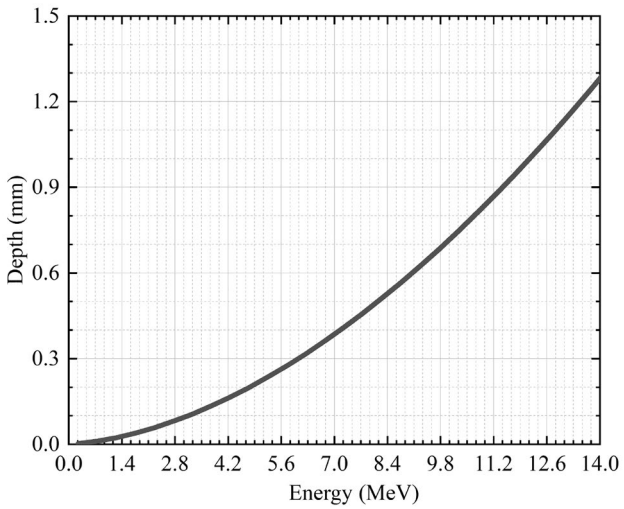

Fig. 4 Detector thickness required for the full deposition of fast neutrons below 14 MeV at vertical incidence

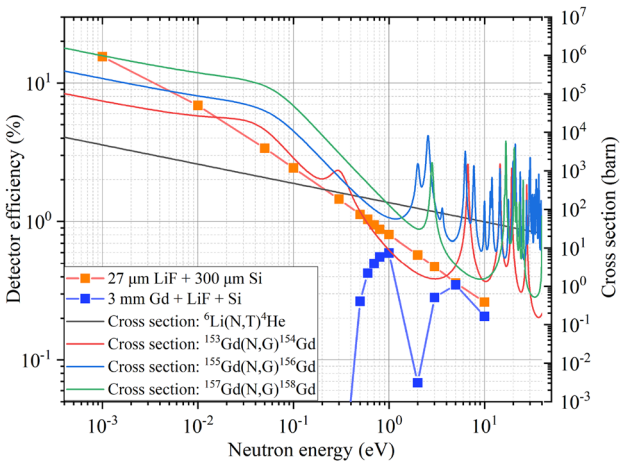

Fig. 6 (Color online) Effect of Gd on thermal neutron detection at different energies

energy. The other lines represent the reaction cross sections of neutrons captured by various Gd isotopes as a function of neutron energy. For thermal neutrons with energies lower than 0.4 eV, the 3 mm-thick Gd can completely block them. The blocking effect of Gd on neutrons of different energies was considered a function of the detection efficiency in subsequent calculations of the orbital thermal neutron flux using neutron spectrometer data.

3 System design

3.1 Hardware design

The hardware design of the neutron spectrometer consists of three circuit boards: a power-supply board, front-end board, and data board. The power-supply board is designed as a low-noise power-supply module that supplies power to all parts of the neutron spectrometer and generates the high-bias voltage required for detector operation. The front-end board is connected to the detector, and the SKIROC2A chip is used as the core of the front-end readout system [44]. The SKIROC2A is a 64-channel front-end ASIC designed to read signals from silicon detectors. The data board contains FPGA, MCU, and memory chips. A physical diagram of the neutron spectrometer is shown in Fig. 7. An overall hardware block diagram is shown in Fig. 8.

The signals from the detector are directly transmitted to SKIROC2A. Then, SKIROC2A converts the analog signals to digital signals and passes them to the FPGA for data processing. Finally, the FPGA passes the processed data to the MCU. Simultaneously, the signals in SKIROC2A are directly connected to the MCU. The MCU is equipped with a CAN interface chip, an Ethernet interface, a USB interface, a UART interface, and an SD NAND. The CAN and Ethernet

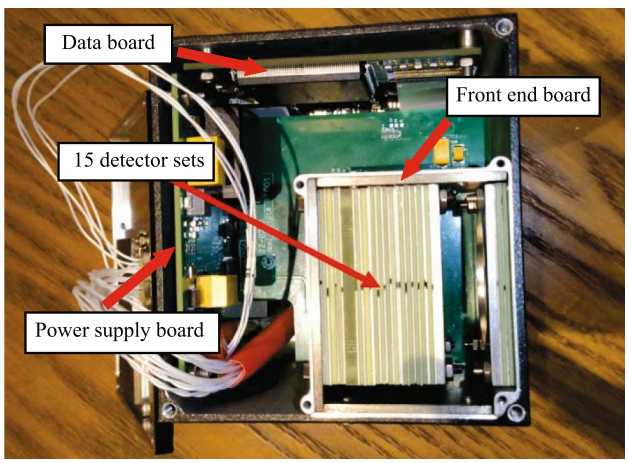

Fig. 7 (Color online) Physical view of neutron spectrometer

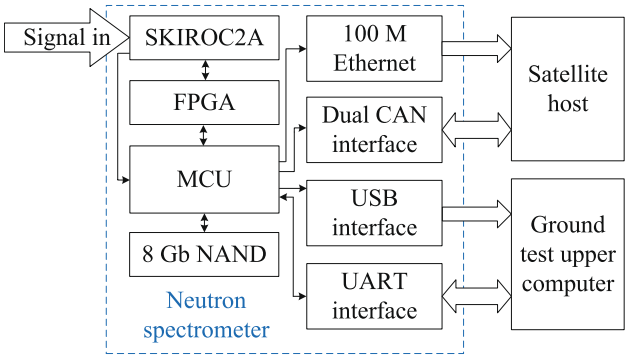

Fig. 8 (Color online) Block diagram of neutron spectrometer hardware

interfaces are used to communicate with the satellite host. CAN transmits commands and telemetry signals, and the Ethernet interface is used to transmit scientific data.

3.2 Firmware design

The firmware design of the neutron spectrometer is implemented using a cyclone series FPGA from Altera. The main purpose of this part is to control SKIROC2A and packetize the data. As the data format of SKIROC2A cannot be changed, the neutron spectrometer uses only 15 of the 64 channels of SKIROC2A; therefore, there is considerable invalid information in the data packet. To reduce the bandwidth and storage pressures, it is necessary for the FPGA to sort valid information from the memory map of SKIROC2A and organize it into data packets, which are ultimately passed to the file management system of the MCU for storage. The firmware design part of the FPGA consists of several modules, including a clock module, a trigger module, a timing control module, a data acquisition module, and an SPI module. A block diagram of the primary modules in the firmware design section is presented in Fig. 9.

The clock module generates clock frequencies of 40 MHz, 5 MHz, 160 MHz, and 2.5 MHz, of which 40 MHz and 5 MHz are used in normal operation, and 160 MHz and 2.5 MHz are used in testing. The trigger module is used for

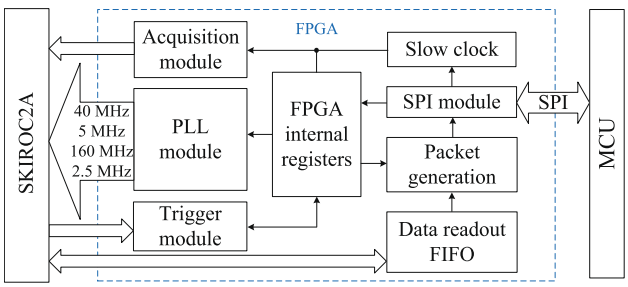

Fig. 9 (Color online) Block diagram of the firmware design module

test calibration. When SKIROC2A generates a trigger signal, the trigger module controls the external ADC to perform the A/D conversion of the charge stored in SKIROC2A. As an external ADC is not used during normal operation, the module is idle. The timing control module must receive and save the slow-control signal for MCU conversion. Before starting the acquisition, the module sends the stored slow-control commands to SKIROC2A and controls the timing of the single-ended signals. The data acquisition module is used to temporarily store the memory map of SKIROC2A, extract valid data, and organize them into packets. The SPI module is used for communication between the FPGA and the MCU.

3.3 Software design

The software design for the neutron spectrometer is realized using the MCU of STM32 series and FreeRTOS. A block diagram of the software design is shown in Fig. 10.

The software design contains four main task threads: the FPGA communication processing thread, interface communication thread, memory system thread, and instruction analysis and telemetry generation thread. In addition to what is shown in the figure, the MCU program includes basic programs, such as the watchdog and clock subroutines.

The FPGA communication processing thread is used to communicate with the FPGA, and includes SPI initialization, slow-control command generation, data processing, and data saving. The interface communication thread is used to control the interfaces with the external devices, including the USB and UART interfaces for ground testing, the two CAN interfaces for connecting to the satellite, and the Ethernet interface for direct digital transmission with the satellite. The storage system interface is used to drive the SD NAND flash memory inside the neutron spectrometer and provide file system services. The file system adopted is FAT32. The command analysis and telemetry generation thread is used to analyze the commands in the CAN and control other threads. The Star Control Center computer sends fast- and slow-change telemetry polling control sequences over the CAN bus to determine the operating status of the neutron spectrometer.

4 System testing and analysis

4.1 Basic performance test

After completing the hardware, firmware, and software designs of the system, it is necessary to test and verify whether the basic performance of the neutron spectrometer meets the design requirements, including the baseline noise RMS, the stability of the neutron spectrometer, consistency between channels, and other basic parameters. In this study, the front-end board is connected to the detector, and the SKIROC2A chip is used as the core of the front-end readout system. Therefore, it is necessary to ensure the baseline RMS noise, the stability of the 64 channels of the SKIROC2A, and the consistency between the channels, which will significantly affect the measurement of the deposition energy spectrum. In the baseline test, the threshold value was set to 255. When the threshold value was close to the baseline reading of the ADC, the trigger circuit continuously generated a trigger signal, acquired and recorded the baseline signal of the 64 channels, and converted it to a numerical value through the internal ADC. Then, the baseline signals of the 64 channels were Gaussian-fitted, and the ADC value where the peak was located was taken as the effective value of the channel

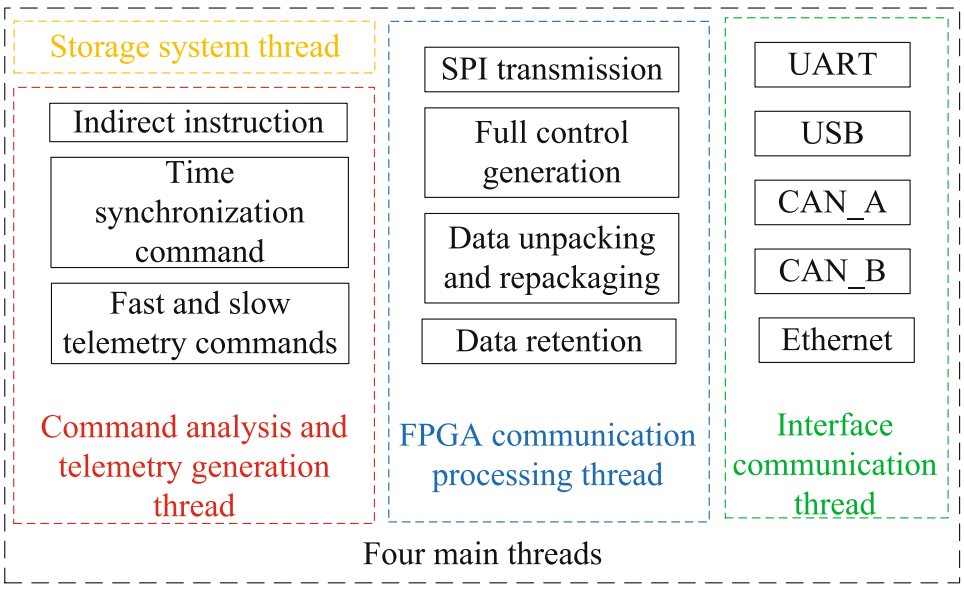

Fig. 10 (Color online) MCU combined with FreeRTOS software design of the four main threads

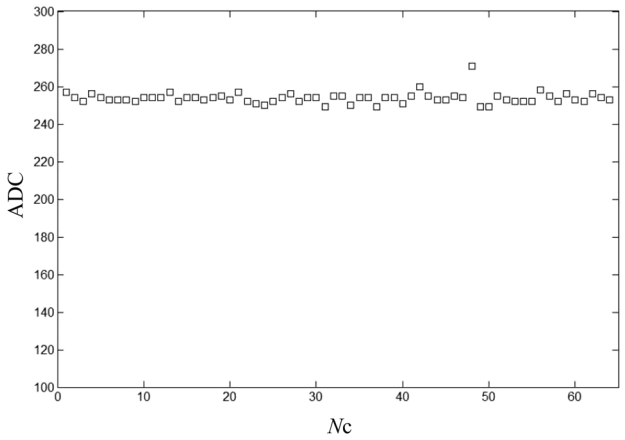

Fig. 11 ADC value of 64-channel baselines

baseline [45]. The ADC values of the 64-channel baselines were obtained as shown in Fig. 11, where the horizontal axis represents the number of channels *Nc*, and the vertical axis represents the ADC readings of the effective value of the baseline over time.

The baselines of most channels were concentrated between 250 and 265, and the baseline difference between different channels was less than 17 ADC values, which showed that the consistency between channels was good. As the SKIROC2A chip is a 12-bit ADC, and the voltage range was 0.9 V to 2.6 V, the RMS noise of the baseline of all the channels was approximately 7.1 mV, and the stability was good. In summary, the baseline RMS noise, the stability of the neutron spectrometer, and the consistency between the channels met the requirements of the subsequent experiments.

The average ionization energy of the silicon semiconductor detector used in the neutron spectrometer was 3.6 eV; that is, one electron was ionized per deposition of 3.6 eV energy. According to the relationship between the baseline RMS noise and deposition energy of the silicon semiconductor detector, the minimum deposition energy measurable by the neutron spectrometer could be obtained. The maximum deposition energy measured using the neutron spectrometer was obtained by continuously increasing the input signal through the signal generator until the ADC value was saturated. Finally, the electronic part of the neutron spectrometer could handle an energy range from 500 keV to 20 MeV [45], and the maximum number of events per second was 75, satisfying the requirements of subsequent experiments.

In addition, in the basic performance test, the anti-irradiation performance of the neutron spectrometer was tested, as the hardware was selected as military-grade components, and the software used was the operating system for each set of data to ensure the validity of the data. In addition to processing the bad block of memory, the neutron spectrometer electronics system is guaranteed to work continuously for a long time in an environment of a higher irradiation level.

After completing the basic performance test of the neutron spectrometer, four major tests were performed: the thermal neutron principle test, fast-neutron detection principle test, fast-neutron detection efficiency test, and compliance effect test.

4.2 Thermal neutron detection test

To test the thermal neutron part of the neutron spectrometer in principle, this study used the ^{241}Am-Be neutron source from the Institutional Center for Shared Technologies and Facilities (INEST) of the Hefei Institutes of Physical Science, Chinese Academy of Sciences, to test the Si detector containing the LiF coating. The energy spectrum of the ^{241}Am-Be neutron source [46] is shown in Fig. 12, with energies in the range of 0 MeV to 11 MeV. The primary fast neutrons produced by the neutron source were slowed down by objects, such as walls and experimental platforms, at the test site; the energy was reduced, and some of the fast neutrons were converted into thermal neutrons with lower energy.

A Si detector with ^{6}LiF coating was used in the test. The thickness of the sensitive layer of the Si detector was 300 μm. The sensitive area was a circle with a diameter of 28 mm. The thickness of the LiF coating was approximately 27 μm. The preamplifier used in the experiment was mesytec-MPR-16 L, and the multichannel analyzer was labeled labZY-nanoMCA. The detector was placed in a 2 mm-thick aluminum alloy shielding shell for shading. A copper mesh was used outside the shielding shell to shield from the electromagnetic interference, with the radioactive source and detector positioned at equal heights. The layout of the experimental site is illustrated in Fig. 13.

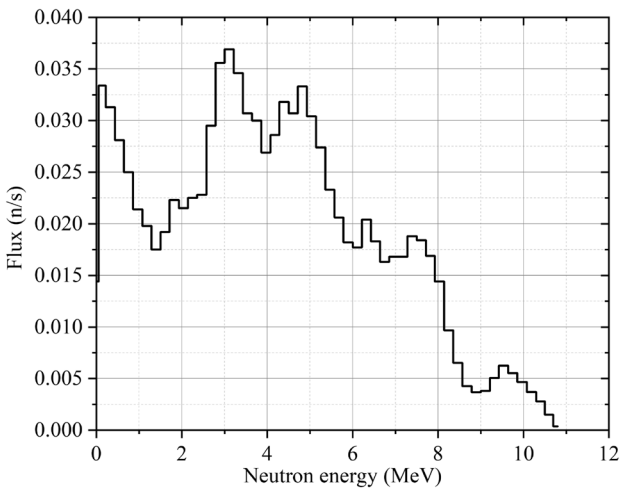

Fig. 12 ^{241}Am-Be neutron source energy spectrum

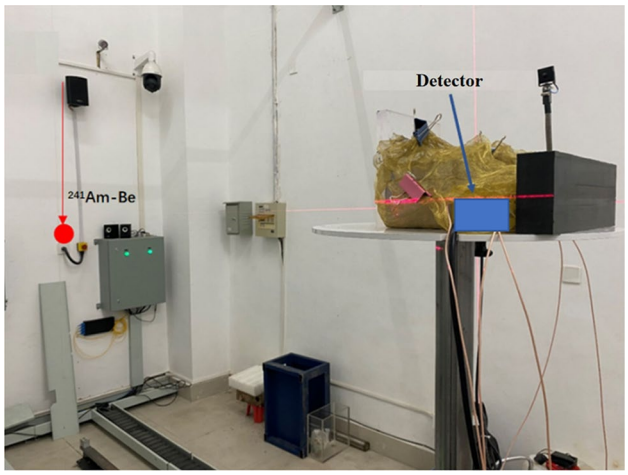

Fig. 13 (Color online) Experimental environment of the ^{241}Am-Be neutron source

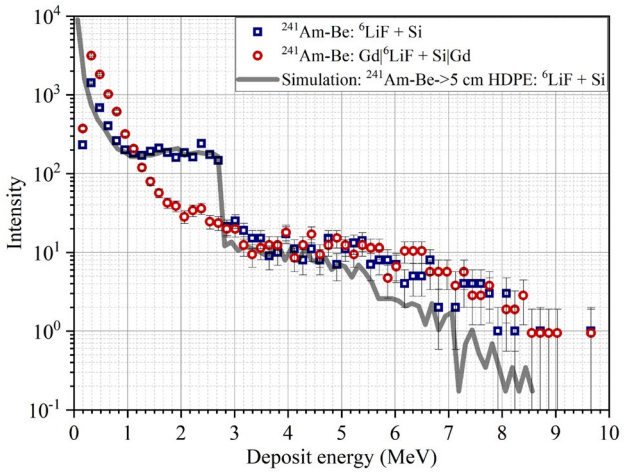

Fig. 14 (Color online) Testing of LiF-coated Si detectors with thermal neutrons after slowing using the ^{241}Am-Be neutron source

The red dots represent ^{241}Am-Be neutron sources. The ^{241}Am-Be neutron source emitted neutrons at a steradian angle of π with a flux of approximately 9×10^7 s^{-1}. The blue part of the back-end experimental platform, which was wrapped in a yellow copper mesh, was a neutron spectrometer. The multichannel spectra obtained from the experiments were energy-scaled to compare the experimental data with the simulation results. The truncation position was at approximately 2.7 MeV in the deposition spectrum, and the starting position of the "platform" was at approximately 1 MeV. The energy spectra from approximately 1 MeV to 2.7 MeV were used for the "platform" integration. The "plateau" integrals were used to normalize the experimental data to the simulated energy spectrum, as shown in Fig. 14.

The blue data points are the multichannel spectral data in the Si detector obtained by using the LiF-coated Si detector and moving the detector so that the distance between the detector and the radioactive source is approximately 50 cm; the red data points are the multichannel spectral data in the Si detector obtained after a period of time based on the experiments on the blue data points, with a piece of Gd with a diameter of 35 mm and a thickness of 3 mm tightly affixed to both sides of the Si detector; the gray line shows the detection effect of the LiF-coated Si detector on the thermal neutrons of the ^{241}Am-Be neutron source slowed down by 5 cm of polyethylene using Geant4. As it is not easy to simulate and reproduce the slowing down effect of neutrons by walls and other objects in an experimental environment, 5 cm-thick polyethylene was used as the neutron-slowing body placed in front of the detector in the simulation.

In the low-energy region below 1 MeV shown in Fig. 14, there are some differences between the blue data points and the simulated energy spectrum, and the experimentally measured low-energy deposited particle signal is greater than that in the simulation, which is caused by electrons produced by ^{241}Am-Be neutrons interacting with Gd. The signals considered in the high-energy part of the experiment were not caused by low-energy thermal neutrons but were produced by ^{241}Am-Be high-energy fast neutrons that directly reacted with the Si nuclei in the Si detector. There are three reasons for the inconsistency between the experimental data and the simulated data. First, the energy spectrum of the ^{241}Am-Be neutron source input to the simulation was a standard energy spectrum, which was different from the actual energy spectrum [47, 48]. Second, as the slowing down effect on neutrons by objects, such as walls, in the experimental environment could not be easily reproduced by the simulation, 5 cm-thick polyethylene was used in the simulation as a neutron-slowing body placed in front of the detector. Finally, the noise signal had an effect owing to the wobbling of the detector's test noise baseline, which was not considered in the simulation [49, 50].

4.3 Principle tests of fast-neutron detection

To perform a principle test of the fast-neutron part of the neutron spectrometer, we tested the Si detector containing an HDPE conversion layer using 2.5 MeV and 14 MeV neutron beams and a ^{241}Am-Be neutron source from INEST.

4.3.1 Testing with 14 MeV monoenergetic neutron beams

The 14 MeV monoenergetic neutron beam of INEST utilizes the deuterium–tritium reaction T(D,N)^{4}He, and the generated neutrons are emitted outward with a stereo angular distribution of approximately 4π centered on the tritium target point. A Si detector with a sensitive area of diameter 28 mm

and thickness 300 μm was used in the experiment in combination with 300 μm-thick HDPE for testing. The preamplifier used in the experiment was mesytec-MPR-16 L, and the multichannel analyzer was labeled labZY-nanoMCA. The experimental site plan and placement of the Si detector are shown in Fig. 15.

The position of the Si detector was approximated to be on a horizontal plane with the target approximately 1.56 m apart. Two control experiments were performed, and the measured multichannel spectral data are shown in Fig. 16.

The black line is the multichannel spectrum generated by the 14 MeV neutron direct bombardment of the Si detector, the red line is the multichannel spectrum generated by the 14 MeV neutron bombardment of the Si detector covered with a 300 μm-thick HDPE conversion layer, and the blue line is the difference between the two, with the black and red lines normalized by the peaks near the last 15,500 channels.

To analyze the experimental data, the total deposition energy spectrum produced by a 14 MeV neutron beam on the Si detector and the effect of the HDPE conversion layer on the total deposition energy spectrum were simulated using Geant4, as shown in Fig. 17.

The black line is the multichannel spectrum produced by 14 MeV neutrons in the Si detector, the red line is the multichannel spectrum produced by 14 MeV neutrons bombarding the Si detector covered with a 300 μm-thick HDPE conversion layer, and the blue line is the difference between the two, where the recoil proton signals produced by the reaction between the neutrons and hydrogen in the HDPE conversion layer can be observed. The black line in Fig. 16 shows the measured multichannel spectrum, and the black line in Fig. 17 shows the simulated energy spectrum, which is different because the walls and other objects in the environment, the problem of energy discrimination in the detector, and the effect of noise signals generated by the wobbling

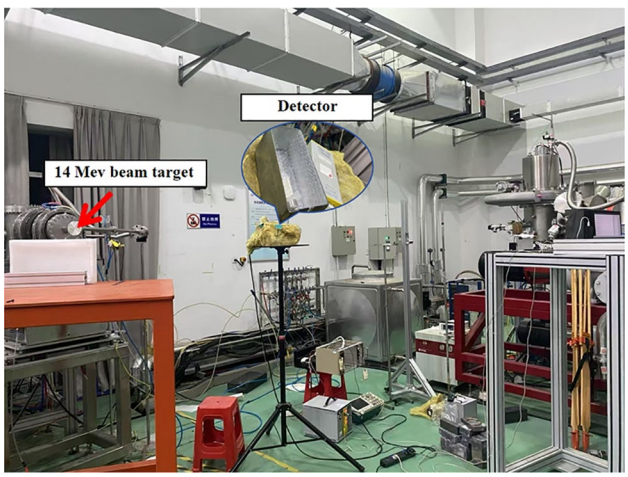

Fig. 15 (Color online) 14 MeV neutron beam test site

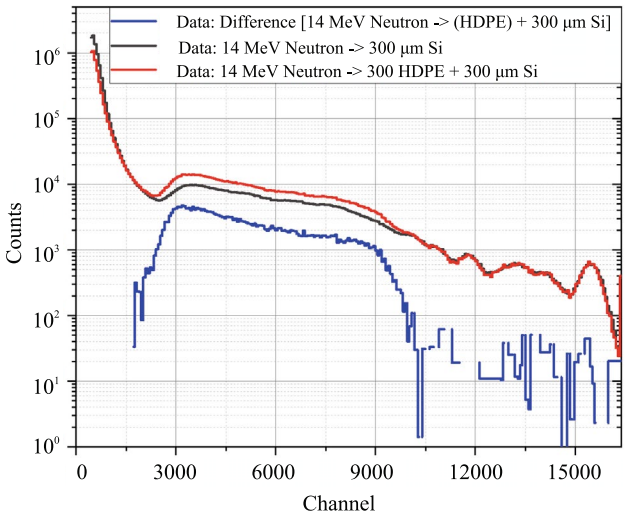

Fig. 16 (Color online) Data from two control experiments of 14 MeV neutron beam flow

of the detector's test noise baseline during the actual test were not considered in the simulation.

Based on the number of channels at the apex of the descending left edge of the recoil proton multichannel spectrum in the experimental data shown in Fig. 16 and at the truncation behind it with the energy values of the corresponding positions in the energy spectrum of the recoil proton in Fig. 17 to the energy scale, the experimentally measured energy spectrum of the recoil proton is obtained, as shown in Fig. 18.

The black data points represent the measured data. The blue lines represent the simulation results for Geant4. The experimental data and simulation results were in

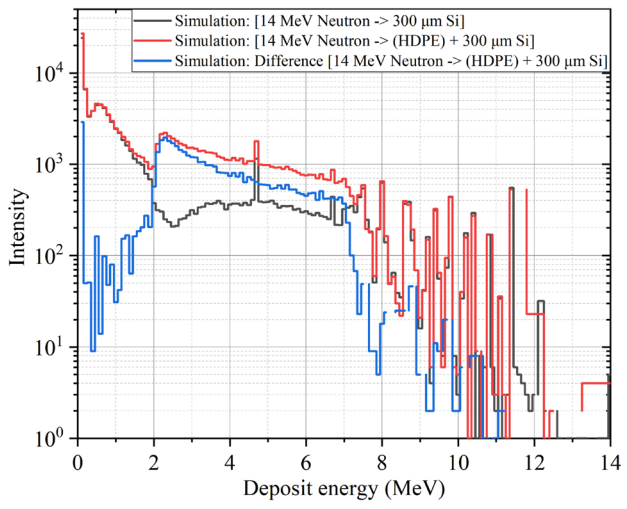

Fig. 17 (Color online) Experimental data of 14 MeV neutron beam simulation using Geant4

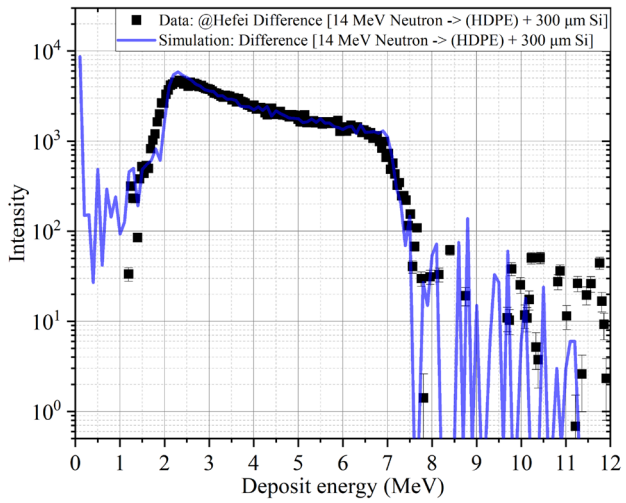

Fig. 18 (Color online) Deposition energy spectrum of recoil protons in a 300 μm-thick Si detector

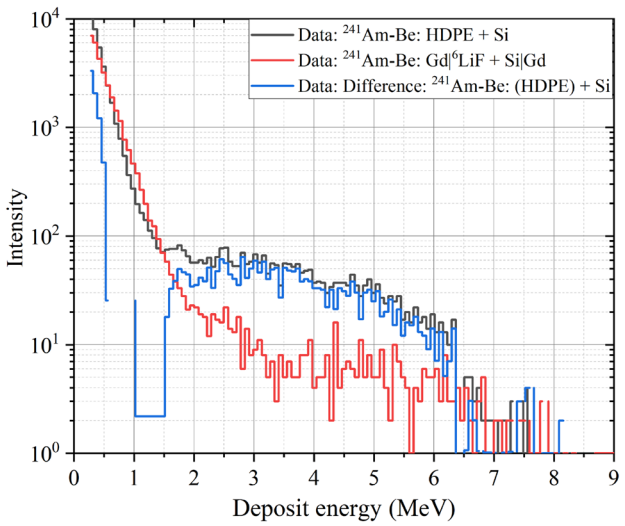

Fig. 19 (Color online) Testing the fast-neutron detection section using the ^{241}Am-Be neutron source

good agreement. As the resolution of the detector was not included in the simulation, the signal peaks of some reactions were narrower than those in the experimental results.

4.3.2 ^{241}Am-Be neutron source test

The experimental setup is illustrated in Fig. 13. In this study, a Si detector with a sensitive region diameter of 35 mm and a sensitive layer thickness of 300 μm was used in combination with a 300 μm-thick HDPE conversion layer for testing. The preamplifier used in the experiment was mesytec-MPR-16 L, and the multichannel analyzer was labeled labZY-nanoMCA. The multichannel spectrum of the Si detector was recorded after the measurement period, as shown in Fig. 19.

The black line is the deposition spectrum of ^{241}Am-Be neutrons in the Si detector shielded by two 3 mm-thick Gd plates, and the red line is the deposition spectrum of ^{241}Am-Be neutrons in the Si detector covered by a 300 μm -thick HDPE conversion layer. The blue line represents the difference between the two. The black and red lines were normalized to the energy spectrum integral from 0.5 MeV to 1 MeV.

The total deposition energy spectrum produced by ^{241}Am-Be neutrons on the Si detector and the effect of the HDPE conversion layer on the total deposition energy spectrum simulated using Geant4 are shown in Fig. 20.

The black line represents the deposition spectrum of ^{241}Am-Be neutrons in the Si detector, and the red line represents the deposition spectrum of ^{241}Am-Be neutrons bombarding the Si detector covered with a 300 μm-thick HDPE conversion layer. The blue line represents the difference between the two. The recoil proton signal is produced by the reaction of neutrons and hydrogen in the HDPE conversion layer. The measured recoil proton spectra are compared with the simulation results, as shown in Fig. 21.

The black data points represent the measured data. The blue line represents the simulation result of Geant4. The experimental and simulated energy spectra between 1.5 MeV and 7 MeV are in good agreement. The reason for the poor agreement in the low-energy region is speculated to be the influence of background noise, such as gamma, in the experiment, which led to poor normalization of the data from the two experiments.

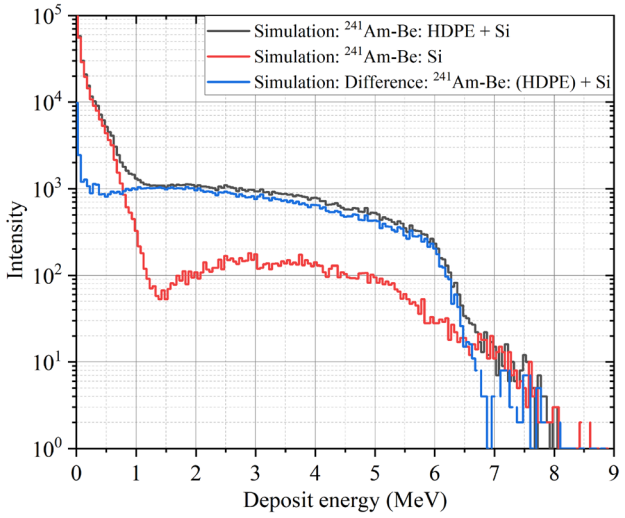

Fig. 20 (Color online) Total deposited energy spectrum of the ^{241}Am-Be neutron source on the Si detector and the influence of the HDPE conversion layer on the total deposited energy spectrum

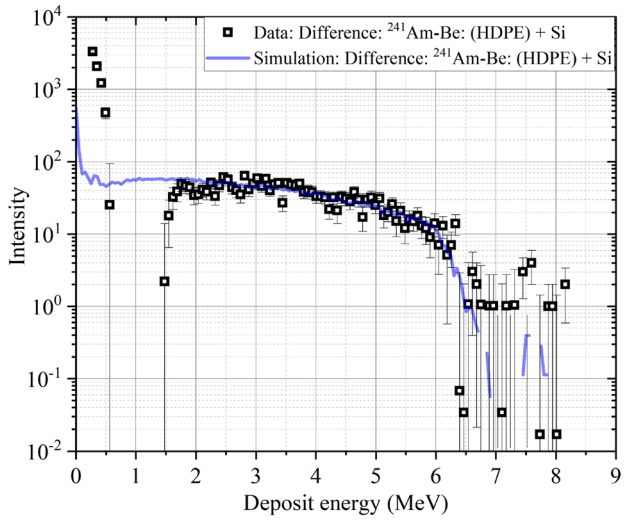

Fig. 21 (Color online) ^{241}Am-Be neutron source bombarding a 300 μm-thick HDPE conversion layer, resulting in a back-scattered proton deposition spectrum in a 300 μm-thick Si detector

4.4 Fast-neutron detection efficiency tests

To test the detection efficiency of the neutron spectrometer for fast neutrons, we used 2.5 MeV and 14 MeV neutron beam from INEST to test a 300 μm-thick Si detector containing a 300 μm-thick HDPE conversion layer. The preamplifier used in the experiment was mesytec-MPR-16 L, and the multichannel analyzer was labeled labZY-nanoMCA.

This study used the data shown in Figs. 16 and 18 to calculate the neutron spectrometer detection efficiency for 14 MeV fast neutrons. The total flux of the neutron source at the target is known. The neutron flux hitting the Si detector was calculated based on the area of the Si detector and the distance from the target. The signal produced by the recoil protons from the reaction of fast neutrons with hydrogen nuclei in the conversion layer of the detector was measured, and the number of fast neutrons measured by the detector was counted. In the experiment, the Si detector and target were approximately on the same horizontal plane, with a linear distance of approximately 1.56 m. The detector was irradiated with a 14 MeV neutron beam with a flux of 2.3×10^{10} s^{-1}. HDPE was placed in front of the detector and irradiated for 20 min to obtain the multichannel spectrum indicated by the black line in Fig. 15. The intrinsic detection efficiency of the detector for 14 MeV fast neutrons was 1.05 %. The detection efficiency is defined as the ratio of the number of signals exceeding the threshold in the detector to the number of neutrons arriving at the detector. The number of neutrons reaching the detector was obtained from the neutron beam flux and the distance of the detector from the beam target, considering that neutrons are generated isotropically.

Correspondingly, we also compared the simulated detection efficiencies at different energy cutoff thresholds, as indicated by the brown line in Fig. 22. The black data points represent the detection efficiencies measured based on the experimental data, and the experimental data and simulation results are in good agreement.

4.5 Coincidence test

To test the compliance effect, a neutron spectrometer was used for the 14 MeV neutron beam stream at the China Institute of Atomic Energy Sciences (CIAES). The placement of the beam pipe and neutron spectrometer at the beam exit of CIAES is shown in Fig. 23. The neutron beam reached

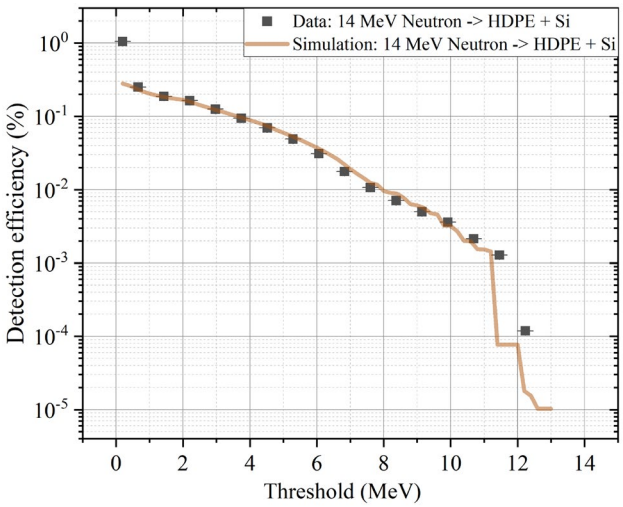

Fig. 22 (Color online) Detection efficiency of a 300 μm Si detector covered with a 300 μm-thick HDPE conversion layer for 14 MeV neutrons

Fig. 23 (Color online) Anti-coincidence test environment

the experimental room through a metal pipeline, and there were a few pieces of equipment in the experimental room. The diameter of the beam spot of the neutron beam was also smaller; therefore, the gamma background of the experimental room was smaller. The neutron spectrometer was placed directly in front of the exit of the neutron beam pipe, and after a period of irradiation, multichannel spectra from multiple detectors in the neutron spectrometer were recorded and analyzed.

In front of Detector No. 7, there was an HDPE conversion layer, where neutrons reacted with the hydrogen nuclei in the conversion layer to produce recoil protons of 0 MeV to 14 MeV [51], which passed through the silicon detector to produce deposition energy. In addition, a corresponding simulation was performed using Geant4 following the same experimental configuration. Figure 24 shows the relationship between the total deposition energy in detectors No. 7 and 8 and the deposition energy in detector No. 7 for each event. Geant4 was used to simulate a certain number of neutrons with an energy of 14 MeV incident vertically from the front of detector No. 1 to the neutron spectrometer, where the colors represent the number of events. Figure 25 shows the data measured under the same conditions. Two bands are evident in both plots when compared. The upper band with a decreasing trend represents those recoil protons that only penetrate detector No. 7 and not detector No. 8. The horizontal coordinate in this case is the total energy of the recoil protons E, and the vertical coordinate is the energy ΔE that the recoil proton loses in detector No. 7 after it penetrates the detector, due to the fact that for the protons with energies higher than 60 keV in the penetration, the energy lost per unit length

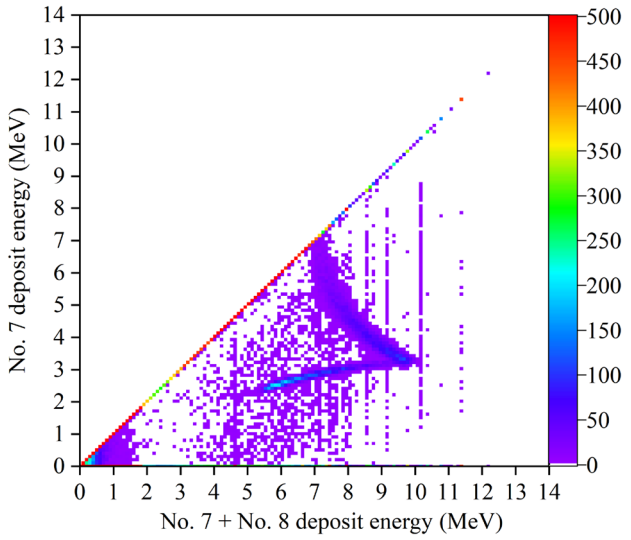

Fig. 24 (Color online) Simulated data for recoil protons detected by the 14 MeV neutron incident neutron spectrometer

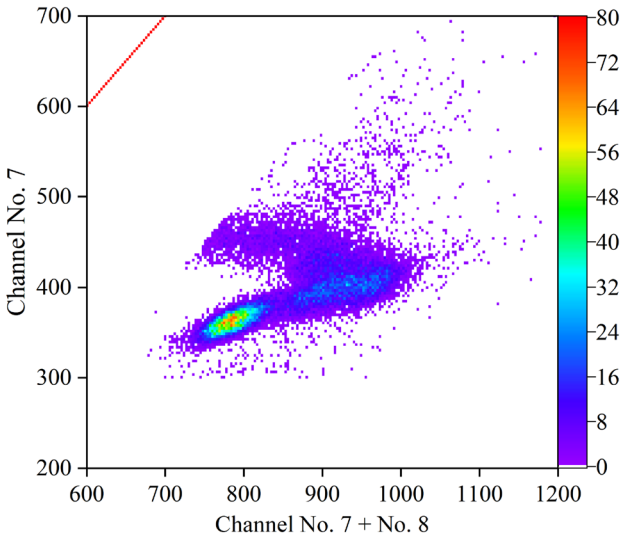

Fig. 25 (Color online) Recoil proton test data detected by the 14 MeV neutron incident neutron spectrometer

in Si decreases monotonically with the increase in the proton energy; hence, the energy lost by the recoil proton in detector No. 7 in this case decreases with the increase in the total energy lost by the recoil proton in both detectors No. 7 and 8. The bands with an upward trend in the lower part represent those that have penetrated both detectors No. 7 and 8. The lower band with an upward trend represents the recoil protons that have penetrated both detectors No. 7 and 8, and the horizontal coordinate in this case is the total energy ΔE_2 lost by the recoil protons in detectors No. 7 and 8 after they penetrate them; the vertical coordinate is the energy ΔE_1 lost by the recoil protons after they penetrate detector No. 7, and ΔE_1 increases with an increase in ΔE_2 in the case of both penetrations.

Because of the difference between the energy and channel correspondences of the two detectors in the actual measurements and the effect of the detector energy resolution, the recoil proton bands in the two-dimensional plots of the measured data are not as concentrated as those in the two-dimensional plots of the simulated results; nevertheless, they are clear enough to show the relationship between the ΔE of the proton in the Si detector and the total energy E. The results also showed that a particle penetrating more than one detector simultaneously can be extracted from the neutron signal using the back-compliance method. The experiment also showed that the event of a particle penetrating multiple detectors can be measured simultaneously, which can guarantee the subsequent extraction of the neutron signal by the inverse conformal method.

5 Summary

In this study, a prototype neutron spectrometer payload for an LEO neutron detection mission was designed and completed. Starting with the detector combination, two combinations of 15 silicon detectors were used, and the hardware, firmware, and software designs of the neutron spectrometer were completed. In this process, we completed the thermal neutron principle test and detection efficiency test using the nuclear reaction method with 27 μm-thick ^{6}LiF as the thermal neutron conversion layer, and the fast-neutron principle test and detection efficiency test with 14 MeV and below, using the nuclear recoil proton method with 300 μm-thick HDPE as the fast-neutron conversion layer. A corresponding simulation analysis of the experiment was performed, and the experimental data and simulation results were in good agreement and met the design expectations. The intrinsic detection efficiency of the probes used in the neutron spectrometer was 1.05 % for 14 MeV fast neutrons. Neutron spectrometers are expected to detect atmospheric albedo neutrons and lightning neutrons in orbit, identify lightning neutrons and atmospheric albedo neutrons based on the spatial distribution of lightning occurrences, and obtain their relative contributions.

Acknowledgements The authors would like to thank the staff of the "Institutional Center for Shared Technologies and Facilities of INEST, HFIPS, CAS," "Division of Ionizing Radiation Metrology, National Institute of Metrology (NIM), China," CIAE, and CSNS Back-n white neutron facility for the grateful support during the measurement.

Author Contributions All authors contributed to the study conception and design. Material preparation, data collection, and analysis were performed by Xiao-Li Wang, Shu-Cheng Shi, Chen-Yao Han, and Yi-Ming Ma. The first draft of the manuscript was written by Chen-Yao Han and Yi-Ming Ma, and all authors commented on previous versions of the manuscript. All authors read and approved the final manuscript.

Data Availability The data that support the findings of this study are openly available in Science Data Bank at https://cstr.cn/31253.11.sciencedb.j00186.00789 and https://doi.org/10.57760/sciencedb.j00186.00789.

Declarations

Conflict of interest The authors declare that they have no conflict of interest.

References

1. B. Klecker, Energetic particle environment in near-Earth orbit. Adv. Space Res. **17**, 37–45 (1996). https://doi.org/10.1016/0273-1177(95)00510-L
2. P. Jiggens, C. Clavie, H. Evans et al., In situ data and effect correlation during September 2017 solar particle event. Space Weather **17**, 99–117 (2019). https://doi.org/10.1029/2018SW001936
3. S.F. Singer, Trapped albedo theory of the radiation belt. Phys. Rev. Lett. **1**, 300 (1958). https://doi.org/10.1103/PhysRevLett.1.181
4. M.I. Dobynde, Y.Y. Shprits, Radiation environment created with GCRs inside a spacecraft. Life Sci. Space Res. **24**, 116–121 (2020). https://doi.org/10.1016/j.lssr.2019.09.001
5. Z. Kopal, Physics of the Sun. Br. J. Appl. Phys. **7**, 119 (1956). https://doi.org/10.1088/0508-3443/7/4/301
6. L. Heilbronn, K. Frankel, K. Holabird et al., Production of neutrons from interactions of GCR-ldce particles. Acta Astronaut. **42**, 363–373 (1998). https://doi.org/10.1016/S0094-5765(98)00131-3
7. L.P. Babich, Generation of neutrons in giant upward atmospheric discharges. JETP Lett. **84**, 285–288 (2006). https://doi.org/10.1134/S0021364006180020
8. W. Xu, S. Celestin, V.P. Pasko, Monte Carlo simulation of neutron generation by lightning leaders. J. Geophys. Res. Space Physics **120**, 1355–1370 (2015). https://doi.org/10.1109/USNC-URSI-NRSM.2013.6525017
9. R.S. Selesnick, M.D. Looper, R.A. Mewaldt, A theoretical model of the inner proton radiation belt. Space Weather **5**, S04003 (2007). https://doi.org/10.1029/2006SW000275
10. J.F. Valdés-Galicia, Y. Muraki, K. Watanabe et al., Solar neutron events as a tool to study particle acceleration at the Sun. Adv. Space Res. **43**, 565–572 (2009). https://doi.org/10.1016/j.asr.2008.09.023
11. H.Y. Huang, Z.Y. Zou, J.H. Hu et al., Characteristics of radiation belt energetic protons and the movement of their core location in response to geomagnetic disturbances. Phys. Fluids **36**, 076601 (2024). https://doi.org/10.1063/5.0216361
12. X.L. Li, R. Selesnick, Q. Schiller et al., Measurement of electrons from albedo neutron decay and neutron density in near-Earth space. Nature **552**, 382–385 (2017). https://doi.org/10.1038/nature24642
13. X.X. Yu, H. Lu, G.T. Chen et al., Detection of solar neutron events and their theoretical approach. New Astron. **39**, 25–35 (2015). https://doi.org/10.1016/j.newast.2014.12.010
14. K. Koga, Y. Muraki, S. Masuda et al., Measurement of solar neutrons on 05 March 2012, using a fiber-type neutron monitor onboard the attached payload to the ISS. Sol. Phys. **292**, 115 (2017). https://doi.org/10.1007/s11207-017-1135-y
15. T. Enoto, Y. Wada, Y. Furuta et al., Photonuclear reactions triggered by lightning discharge. Nature **551**, 481–484 (2017). https://doi.org/10.1038/nature24630
16. L.P. Babich, Radiocarbon production by thunderstorms. Geophys. Res. Lett. **44**(191–11), 200 (2017). https://doi.org/10.1002/2017GL075131
17. Q.Q. Shi, C.Y. Han, Q.G. Zong et al., Lightning-induced neutrons as a possible source of charged particles in the Earth's inner radiation belt. Earth Planet. Phys. **9**(2), 444–451 (2025). https://doi.org/10.26464/epp2025014
18. J.E. Keith, G.D. Badhwar, D.J. Lindstrom, Neutron spectrum and dose-equivalent in shuttle flights during solar maximum. Nucl. Tracks Radiat. Meas. **20**, 41–47 (1992). https://doi.org/10.1016/1359-0189(92)90083-8
19. V.E. Dudkin, Y.V. Potapov, A.B. Akopova et al., Differential neutron energy spectra measured on spacecraft in low earth orbit. Nucl. Tracks Radiat. Meas. **17**, 87–91 (1990). https://doi.org/10.1016/1359-0189(90)90188-4
20. A.M. Preszler, S. Moon, R.S. White, Atmospheric neutrons. J. Geophys. Res. **81**, 4715–4722 (1976). https://doi.org/10.1029/JA081i025p04715
21. V.I. Lyagushin, V.E. Dudkin, Y.V. Potapov et al., Russian measurements of neutron energy spectra on the Mir orbital station. Radiat. Meas. **33**, 313–319 (2001). https://doi.org/10.1016/S1350-4487(00)00156-6
22. H. Matsumoto, T. Goka, K. Koga et al., Real-time measurement of low-energy-range neutron spectra on board the space shuttle

STS-89 (S/MM-8). Radiat. Meas. **33**, 321–333 (2001). https://doi.org/10.1016/S1350-4487(00)00157-8
23. G.H. Shen, S.Y. Zhang, X.G. Zhang et al., Using energy particle detection technology on the Tiangong's space station's Wentian laboratory cabin module. Aerospace **10**, 373 (2023). https://doi.org/10.3390/aerospace10040373
24. G.H. Shen, D.H. Hou, Y. Chang et al., Neutron observations from the energetic particle detector on China's Space Station. Earth Planet. Phys. **9**(2), 460–466 (2025). https://doi.org/10.26464/epp2024078
25. Z.L. Tang, M. Shen, Performance test and evaluation for pixel CdZnTe detector of different thickness. Adv. Mat. Res. **1015**, 101–104 (2014). https://doi.org/10.4028/www.scientific.net/AMR.1015.101
26. L.Y. Liu, X. Ouyang, R.L. Gao et al., Latest developments in room-temperature semiconductor neutron detectors: prospects and challenges. Sci. China Phys. Mech. Astron. **66**, 232001 (2023). https://doi.org/10.1007/s11433-022-2021-6
27. W. Gao, S. Li, Y. Duan et al., Design and characterization of a low-noise front-end readout ASIC in 0.18-m CMOS technology for CZT/Si-PIN detectors. IEEE Trans. Nucl. Sci. **65**, 1203–1211 (2018). https://doi.org/10.1109/TNS.2018.2826070
28. S. Zhao, C. Gao, X. Tian et al., A high counting-rate readout ASIC for CZT detectors. Nucl. Instrum. Methods Phys. Res., Sect. A. **1064**, 169416 (2024). https://doi.org/10.1016/j.nima.2024.169416
29. R. He, X.Y. Niu, Y. Wang et al., Advances in nuclear detection and readout techniques. Nucl. Sci. Tech. **34**, 205 (2023). https://doi.org/10.1007/s41365-023-01359-0
30. X. Zhu, C.Q. Feng, Q. Li et al., FPGA-based real-time n/γ discrimination with liquid scintillator. IEEE Trans. Nucl. Sci. **65**, 2877–2882 (2018). https://doi.org/10.1109/TNS.2018.2877598
31. Y.P. Cheng, W.L. Guo, Z.Y. Tang et al., Mission and payload design for in-situ detection of lunar regolith neutron radiation environment. J. Space Sci. Exp. **1**, 63–71 (2024)
32. C.J. Stapels, E.B. Johnson, X.J. Chen et al., Space neutron spectrometer design with SSPM-based instrumentation. Nucl. Instrum. Methods Phys. Res. A. **652**, 342–346 (2011). https://doi.org/10.1016/j.nima.2010.10.050
33. Z.Y. Zhu, M.Q. Pu, M. Jiang et al., Bonding processing and 3D integration of high-performance silicon PIN detector for ΔE-E telescope. Processes **11**, 627 (2023). https://doi.org/10.3390/pr11020627
34. S.N. Wang, M. Yu, D.Y. Tian et al., Fabrication and characterization of thin silicon PIN detectors. ECS Trans. **60**, 1165 (2014). https://doi.org/10.1149/06001.1165ecst
35. C.Y. Han, S. Wang, Q.Q. Shi et al., A background suppression detector array for fast neutron measurement in space science study. Measurement **230**, 114479 (2024). https://doi.org/10.1016/j.measurement.2024.114479
36. C.L. Zhou, S.F. Li, C.X. Xu, Study on influence factors of the peak-to-Compton ratio of the HPGe γ-ray spectrometer system based on the anti-coincidence measuring technique. Nucl. Electron. Detect. Technol. **26**, 429–433 (2006). https://doi.org/10.3969/j.issn.0258-0934.2006.04.011
37. H.M. Gerstenberg, R.S. Caswell, J.J. Coyne, Initial spectra of neutron-induced secondary charged particles. Radiat. Prot. Dosim. **23**, 41–44 (1988). https://doi.org/10.1093/oxfordjournals.rpd.a080126
38. J.Y. Yang, L. Li, H.W. Lyu et al., A calculation method for parameters of secondary neutron source in nuclear reactor. Nucl. Tech. **41**, 060605 (2018). https://doi.org/10.11889/j.0253-3219.2018.hjs.41.060605
39. G.H. Zhang, J.M. Liu, Z.H. Xue et al., Measurement of ^{10}B content in thin-film ^{10}B samples. Appl. Radiat. Isot. **69**, 858–861 (2011). https://doi.org/10.1016/j.apradiso.2011.02.017
40. A. Omar, S. Burdin, G. Casse et al., GAMBE: thermal neutron detection system based on a sandwich configuration of silicon semiconductor detector coupled with neutron reactive material. Radiat. Meas. **122**, 121–125 (2019). https://doi.org/10.1016/j.radmeas.2019.01.019
41. J.S. Wan, G.N. Zhu, Y. Zhao et al., Computer studies of detection efficiency of fast-neutron spectrum based on PADC using the Monte Carlo method. Radiat. Meas. **36**, 193–197 (2003). https://doi.org/10.1016/S1350-4487(03)00122-7
42. Y.M. Ma, Research and design of space neutron detection system. Weihai, China: Shandong University. (2023). https://doi.org/10.27272/d.cnki.gshdu.2023.006159
43. C.Y. Han, Simulation and test of neutron spectrometer in near-Earth orbit. Weihai, China: Shandong University. (2022). https://doi.org/10.27272/d.cnki.gshdu.2022.003927
44. T.Z. Chen, X.H. Li, K. Wang et al., A readout electronic system for a 3D position-sensitive CdZnTe gamma-ray spectrometer based on the CPRE10-32 readout ASIC. J. Instrum. **17**, T10005 (2022). https://doi.org/10.1088/1748-0221/17/10/T10005
45. S.Y. Ma, S.B. Liu, H. Liu et al., A SKIROC2-based prototype electronics system for silicon PIN array. Radiat. Detect. Technol. Methods **2**, 36 (2018). https://doi.org/10.1007/s41605-018-0060-4
46. Y.X. Liu, S. Zhang, Y.K. Qian et al., Monte Carlo simulation study on the ^{241}Am-Be radionuclide source reference neutron radiation. Nucl. Technol. Radiat. Prot. **35**, 283–293 (2020). https://doi.org/10.2298/NTRP2004283L
47. W.H. Zhang, H.B. Kang, Y.J. Wang et al., Development of a portable single sphere neutron spectrometer. Radiat. Meas. **140**, 106509 (2021). https://doi.org/10.1016/j.radmeas.2020.106509
48. P.Q. Wang, J.K. Yang, F. Li et al., Thermal neutron reference radiation facility with high thermalization and large uniformity area. Metrologia **60**, 45002 (2023). https://doi.org/10.1088/1681-7575/acd6fb
49. R. García-Baonza, G.F. García-Fernández, E. Gallego et al., A novel conceptualization in the analysis and design of passive neutron area monitors based on gold foil activation. Appl. Radiat. Isot. **181**, 110110 (2022). https://doi.org/10.1016/j.apradiso.2022.110110
50. R. Tursinah, S. Permana, Z. Su'ud et al., Design and validation of a single cylindrical neutron spectrometer using a gold activation foil. Radiat. Meas. **171**, 107053 (2024). https://doi.org/10.1016/j.radmeas.2024.107053
51. W. Jiang, H.Y. Jiang, H. Yi et al., Detector calibration based on secondary protons at the Back-n white neutron source. Acta Phys. Sin. **70**, 082901 (2021). https://doi.org/10.7498/aps.70.20201823